HOKKAIDO UNIVERSITY

Title	Self-assembly of MoO3 needles in gas current for cubic formation pathway
Author(s)	Ishizuka, Shinnosuke; Kimura, Yuki; Yokoi, Satoki; Yamazaki, Tomoya; Sato, Rikako; Hama, Tetsuya
Citation	Nanoscale, 9(28), 10109-10116 https://doi.org/10.1039/c7nr02613g
Issue Date	2017-06-20
Doc URL	http://hdl.handle.net/2115/70788
Type	article (author version)
Additional Information	There are other files related to this item in HUSCAP. Check the above URL.
File Information	Ishizuka_MoO3_Nanoscale_HUSCAP.pdf

Instructions for use

Journal Name

ARTICLE

Self-Assembly of MoO₃ Needles in Gas Current for Cubic Formation Pathway

Shinnosuke Ishizuka[a], Yuki Kimura[a]*, Satoki Yokoi[b], Tomoya Yamazaki[a], Rikako Sato[a] and Tetsuya Hama[a]

Nucleation and subsequent rapid growth are enigmatic due to the unrevealed pathways. Despite the relatively simpler mechanism than nucleation and growth in solution, that in vapor has received little attentions. The largest hindrance to unveiling this process may be observing the rapid and mesoscopic-scale phenomena. To overcome this hindrance, we combine an experimental approach with in-situ spatial scanning Fourier-transform infrared spectroscopy, which reveals the nucleating and growing nanoparticles in vapor. The nanoparticles are then collected at different evolutionary stages and analyzed by ex-situ transmission electron microscopy (TEM). Needle-shaped molybdenum oxide (MoO₃) nanoparticles were formed within ~0.1 s after homogeneous nucleation from a highly supersaturated vapor. Over one second, the needle particles gradually evolved into a cubic shape by fusion in a crystallographically favored orientation in a free-flying state in vapor. The similar sizes of the elongated axes of the needle and cubic structures suggest an additional growth stage, in which the needle particles become the growth units of the cubic particles. The morphology of a final crystal should reflect the formation environment of the particle because growing crystals are sensitive to the formation conditions such as temperature, concentration, and impurities. Although nucleation under very high supersaturation induces anisotropic growth of the needle particles, this information of the initial nucleation environment is lost in the final cubic crystal. These findings enrich our understanding of pathways in the nucleation and growth of nanoparticles and provide new insights into the growth stages driven by oriented attachment.

1 Introduction

Nucleation critically determines the characters (such as crystalline size, shape, polymorphism, and crystallinity) of inorganic,[1–8] organic,[9–11] proteinaceous,[12,13] and colloidal[14,15] materials. In an ideal system, a crystal grows continuously toward its final form by sequential incorporation of growth units.

In the last decade, in-situ observations have revealed unexpected nucleation pathways, especially in solution systems. These observations have overridden the previous simple view that nucleation proceeds by monomer-by-monomer incorporation of basic units. Before the stable crystal is formed, intermediates such as polymorphs,[3] amorphous solid particles,[3] liquid droplets,[6,7,12,13] clusters with characteristic structures,[4,11] and crystals with different chemical compositions from the final crystal[2] precipitate out as metastable phases. The formation sequence sometimes follows Ostwald's step rule, in which the metastable intermediates precipitate due to lower surface energies than the stable phase.[16] This process is complicated by the characteristics of solvent molecules. To approach a kink site and thereby join the crystal, a growth unit in water must dehydrate the hydrated layer that surrounds the material. Dehydration process plays key roles at the early stage of nucleation and growth in solution.[17,18]

In contrast to complex nucleation from solution, nucleation of inorganic particles from a vapor is surface free, so we expect that the result to be comparable to the nucleation theory. Some experimental studies have attempted to unveil the nucleation process. For instance, after thermal evaporation at extremely high supersaturation, metal and metal oxides nucleate homogeneously in the cooling gas.[19–21] According to nucleation theory, the critical nuclei in manganese nucleation should be several atom/molecules in size, and their surface free energy should be 30% larger than that of the corresponding bulk.[20]

Unexpected pathways in the post-nucleation growth processes have also been proposed. Inter-particle coarsening is thought to determine the resulting characteristics of crystals in some solution systems.[22] When coarsening happens selectively between crystallographically equivalent planes, it is known as oriented attachment growth.[e.g.,2,23–27] For many years, the fusion of two nanoparticles and agglutination by

44 surface melting has been known to dominate the growth
45 process in vapor phase. These previous studies show that
46 nucleation and growth pathways are not simple processes
47 such as continuous incorporation of monomer molecules, but
48 are universally more diverse than hitherto predicted.[26,27]
49   Here we experimentally investigate vapor phase nucleation
50 and subsequent growth of nanoparticles. Our proposed
51 approach captures the early stages of crystallization using in
52 situ spatial scanning spectroscopy by a transmittance Fourier
53 transform infrared (FT-IR) spectrometer. The in-situ IR data
54 (which reflect the chemical compositions, phases, and shapes
55 of the just-nucleated nanoparticles in the free-flying state) are
56 complemented by TEM observations of the collected products.
57 Applied in vapor phase nucleation, this technique
58 demonstrates that morphological evolution of just-nucleated
59 MoO₃ nanoparticles is induced by inter-particle coarsening at
60 crystallographically equivalent planes during frequent
61 collisions in the gas current.

Experimental section

63   Nucleation and subsequent growth experiments of MoO₃
64 nanoparticles in vapor phase were performed in a stainless
65 steel chamber combined with a FT-IR spectrometer (JASCO,
66 VIR200), as described in our previous study.[28] The
67 experimental apparatus for forming nanoparticles in the gas
68 current is schematized in Figure S1a. The thallium bromoiodide
69 (KRS5) viewports provide an optical path for the FT-IR analysis.
70 KRS5 exhibits high transmittance in the 10000–250 cm^{-1} range.
71 The transmitted IR light was sensed by a detector unit
72 comprising an aperture, an IR filter (LP-8335, IR System Co.
73 Ltd., Tokyo, Japan), a parabolic mirror, and an HgCdTe (MCT)
74 photo-conductive detector (P5274-01, Hamamatsu Co.,
75 Shizuoka, Japan). The viewports were fixed to a U-shaped
76 bench on which the FT-IR and detector unit were set at either
77 side of the chamber. The chamber and viewports were
78 connected by flexibly extendable bellows. In addition, the
79 bench was interlocked to withstand a load motor unit
80 (LAS4F40MW-1, Oriental Motor Co., Tokyo, Japan). In this
81 configuration, we could acquire the transmittance FT-IR
82 spectra at different heights from the evaporation source in a
83 single experiment. The measurable region (65 mm along the
84 vertical axis) exceeded the inner diameter of the windows (30
85 mm). The bench height was measured by a laser measurement
86 sensor (CD22, OPTEX FA Co., Kyoto, Japan). The chamber was
87 connected to a turbo-molecular pump (50 L/s). After
88 evacuating the chamber to below 1.0×10^{-4} Pa, the gate valve
89 was closed and high-purity O₂ (99.9%) and He (99.9999%) were
90 injected. The pressure was first to 4.0×10^{2} Pa with O₂ gas,
91 then increased to 5.0×10^{3} Pa with He gas. The gas pressure
92 was measured by a crystal ion gauge (M-601GC, ANELVA Co.,
93 Kanagawa, Japan) at $<10^{-1}$ Pa, and by a piezoresistive pressure
94 sensor (Pressure sensor 680, Huba Control, Switzerland) at >1
95 Pa.
96   The evaporation source was a Mo wire (φ =1 mm, length =75
97 mm, purity 99.95%). The wire was connected to Cu electrodes
98 for rapid electrical-resistance heating. At the starting position

99 in Experiment A and B, the optical axis of the FT-IR was
100 centered at 10 mm beneath and 7.5 mm above the
101 evaporation source, respectively. The temperature of the
102 evaporation source was monitored during the experiments by
103 a radiation thermometer (λ = 0.8–1.6 μm; FTZ2, Japan Sensor
104 Co., Tokyo, Japan). In the temperature calculation, the
105 emissivity of the Mo wire surface was assumed constant at 0.3.
106 However, because the emissivity changes by surface oxidation
107 of the Mo wire, the absolute temperature obtained in this
108 study may depend on the oxygen vapor pressure. The
109 evaporation source was rapidly heated to ~1900 K by applying
110 an AC voltage to the electrodes, then maintained at this
111 temperature throughout each experiment. Once the
112 temperature had stabilized, the bench was moved toward the
113 vertical axis at 10 mm s^{-1}, until the optical path reached 10
114 mm and 67.5 mm above the evaporation source in Experiment
115 A and B, respectively. The bench was then returned to its
116 starting position at 10 mm s^{-1}. Smoke formation was
117 confirmed by a CMOS camera (MS-M33WT3, Mosquell Co.,
118 Ltd., Tokyo, Japan) as shown in Figure S2. When the U-shaped
119 bench began to move, the convection has become stationary,
120 as confirmed by the shape of the smoke. Several seconds after
121 the bench reached its starting position, the AC voltage was
122 turned off. The changes in temperature of the evaporation
123 source, pressure in the chamber and relative distance between
124 the optical axis and the evaporation source were recorded,
125 and the results are plotted in Figure S3 for the Experiment B.
126   Surface oxidation on the Mo wire results in MoO₃ formation.
127 As MoO₃ has higher vapor pressure than Mo metal, the
128 oxidized MoO₃ was simultaneously evaporated as molecules
129 from the evaporation source. The gas flowed upward under
130 thermal convection generated by the evaporation source itself,
131 inducing the homogeneous nucleation of nanoparticles. The
132 nucleation was visible as a smoke. By setting the optical path
133 of the FT-IR just above the evaporation source, we could
134 measure the IR spectra of the nascent condensates in the free-
135 flying state. The aperture diameter was adjusted to improve
136 the spatial resolution at a suitable IR signal intensity. At an
137 aperture diameter of 8 ± 1 mm, the beam diameter at the
138 center of the optical axis (where the nanoparticles were
139 nucleated) was calculated as 4.5 ± 0.6 mm. The measurement
140 region was a column of width 5 mm (Figure S1b). The time
141 evolution of the IR spectra was obtained at 24 spectra/s. The
142 background spectra were obtained at each height from the
143 evaporation source, following the procedure just before the
144 experiment. The signal spectra in each 5-mm region were
145 averaged, and the absorbance spectra were then obtained
146 from 7.5 mm to 67.5 mm above the evaporation source. To
147 confirm the consistency of the region-dependent IR spectra in
148 the smoke, the spatial scan spectra were obtained in both
149 outward and homeward directions.
150   Some ascending nanoparticles were attached to stainless-
151 steel collecting sheets; one fixed at 10 mm beside the
152 evaporation source, the other fixed at more than 250 mm
153 above the evaporation source. The collected particles were
154 picked up on a standard Cu grid sweated with ethanol and
155 dried for 1 minute. The particles were observed by TEM (JEM-
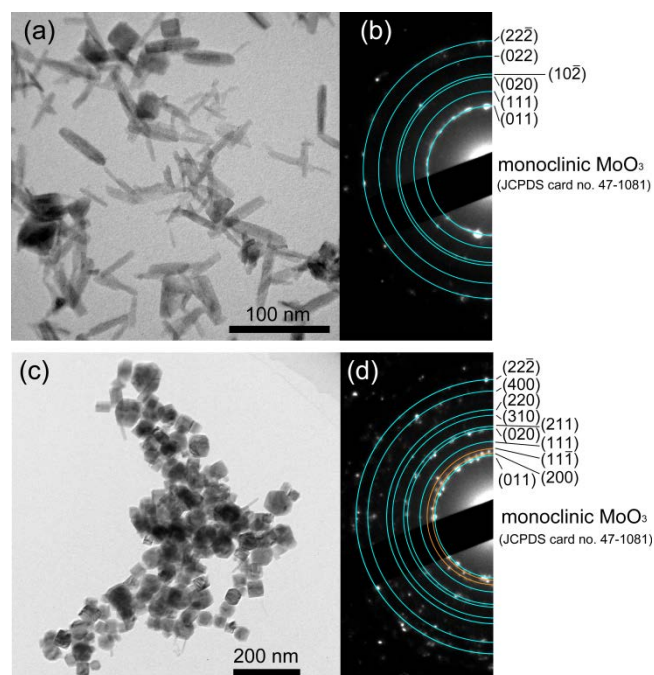
Figure 1. Typical TEM images of the synthesized nanoparticles collected (a) at the height of the evaporation source on the side collector set beside and (c) at the roof collector. (b), (d) electron diffraction (ED) patterns corresponding to (a) and (c), respectively.
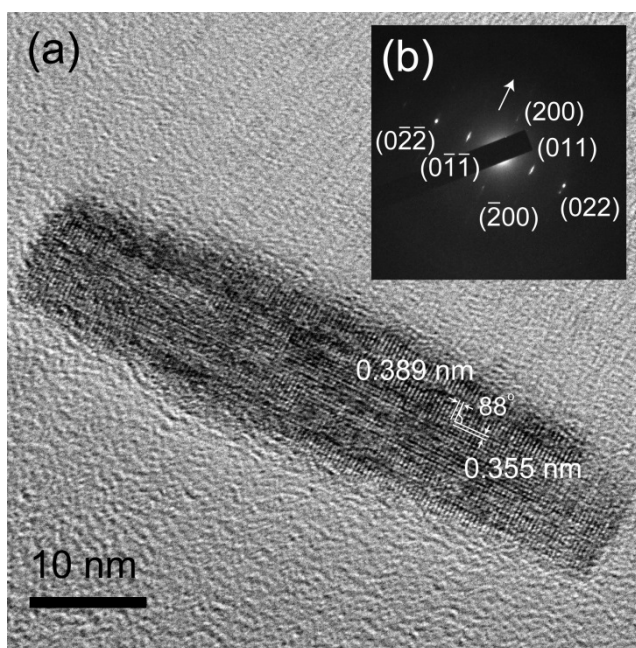

Figure 2. High resolution image of a typical needle shaped particle and (b) its corresponding ED pattern. Streaks along [200] are indicated by the white allow.

156 2100F, JEOL Co., Japan) at an acceleration voltage of 200 kV.
157 The remaining particles on the collecting sheet were agitated
158 with KBr powder and formed into 10 mm-diameter pellets
159 under a pressure of 8×10^4 N for subsequent FT-IR
160 measurements.

Results

162 Molybdenum (Mo) wire was heated in a regulated gas
163 mixture of reactant oxygen (P_{O2} = 4.0×10^2 Pa) and buffer
164 helium (P_{He} = 4.6×10^3 Pa). The oxidation and subsequent
165 evaporation of MoO_3 and the nucleation of nanoparticles were
166 confirmed as visible smoke. Convection carries the evaporated
167 MoO_3 gas around the evaporation source. Consequently, the
168 gas concentration is highest at the bottom of the evaporation
169 source and nucleation is induced at several millimeters
170 beneath the Mo wire. High O_2 partial pressure induces efficient
171 oxidation and evaporation of Mo source. In addition, high total
172 pressure induces frequent collision between the just-nucleated
173 nanoparticles in gas current. These leads increase in size of
174 resulting materials and reduce the time scale for shape
175 evolution.[29] We selected relatively low O_2 partial pressure and
176 total pressure conditions (less frequent collision condition) in
177 order to clarify the particle formation sequences in the spatial
178 resolution of our experimental system. Nucleated MoO_3
179 nanoparticles appear floating in the ascending gas current
180 generated by the hot evaporation source. The MoO_3
181 nanoparticles are then cooled in the convection from
182 nucleation temperature (typically around 1000 K) to room
183 temperature in 1 s. Owing to the rapid heat exchange, the
184 temperature of the nanoparticles in the ascending gas current
185 is similar to that of the surrounding gas.

186 To identify the size, shape, and polymorph changes of the
187 nanoparticles produced in the ascending gas current, we
188 collected the nanoparticles at different heights from the
189 evaporation source and observed them using a TEM. The
190 floating nanoparticles were attached on SUS sheets set at 10
191 mm beside the evaporation source (side collector) and at ~250
192 mm above the evaporation source (roof collector) (Figure S1).
193 Nanoparticles collected at the side collector (placed at the
194 height of the Mo wire) are mainly composed of needle-shaped
195 particles, accompanied by a small number of cubic shaped
196 particles (Fig. 1a). Corresponding electron diffraction (ED)
197 patterns (Fig. 1b) and the crossing angle of the lattice fringes
198 (obtained in high-resolution images of a needle particle; see
199 Fig. 2) consistently matched monoclinic MoO_3 with a unit cell
200 size of a = 7.118 Å, b = 5.366 Å, and c = 5.568 Å (JCPDS card no.
201 47-1081). The needle particles were always elongated along
202 [011]. In contrast, most of the samples collected at the top of
203 the chamber were cubic or polyhedral (Fig. 1c). Though clear
204 distinction between cubic and polyhedral particles were
205 difficult because some cubic particles had roundish edges and
206 irregularly deformed outlines, the number of cubic particles
207 was more dominant than polyhedral particles in all samples.
208 The ED patterns of these particles were also consistent with
209 monoclinic MoO_3 (Fig. 1d). The rings corresponding to $(11\bar{1})$
210 and (200) (indicated by the orange lines in Fig. 1d) do not
211 appear in the ED pattern of the needle-shaped particles in Fig.
212 1b. The needle particles showed well-aligned lattice images of
213 (011), but frequent defects in the perpendicular planes.
214 The lengths of the long and perpendicular (short) axes were
215 measured in samples collected at various heights above the
216 evaporation source (Fig. 3a). The short axis was measured
217 along the middle part of the nanoparticles. The average
218 lengths of the axes (long axis, short axis), measured from at
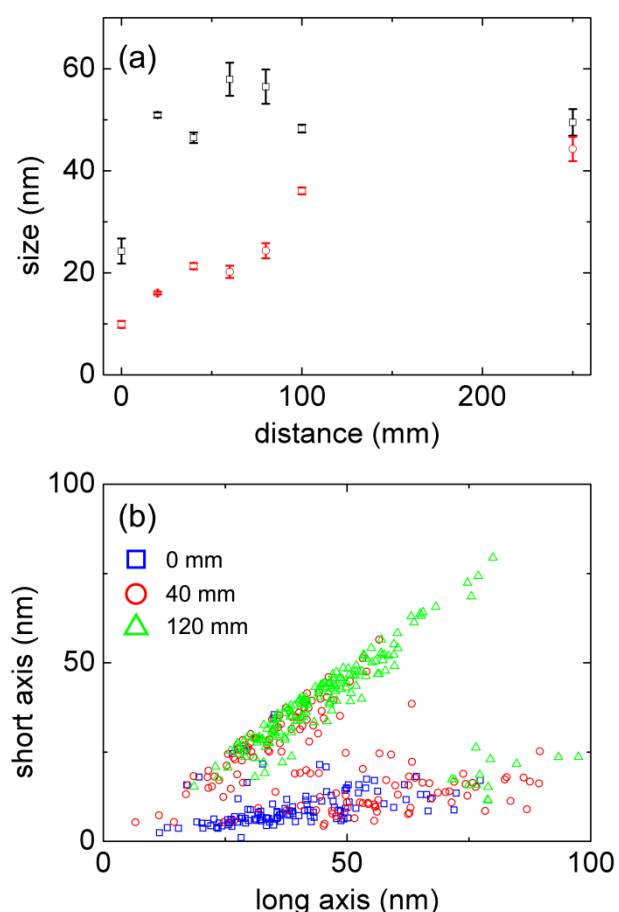219 least 126 particles in each sample, were (24.3 ± 2.5, 9.9 ± 0.7),

Figure 3. (a) Averaged lengths of the long axis (black squares) and short axis (red squares) of the nanoparticles collected at 0, 20, 40, 60, 80, 120 and ~250 mm above the evaporation source, plotted with their error bars, and (b) the size distributions of samples collected at 0 mm (blue squares), 40 mm (red squares) and 120 mm (green squares).

(50.9 ± 0.5, 16.0 ± 0.3), (46.5 ± 1.0, 21.3 ± 0.6), (58.0 ± 3.4, 20.2 ± 1.5), (56.5 ± 3.4, 24.4 ± 1.5), (48.3 ± 0.8, 36.1 ± 0.7), and (49.5 ± 2.6, 44.3 ± 2.4) nm at collection heights of 0, 20, 40, 60, 80, 120, and ~250 mm, respectively. The longitudinal length of the nanoparticles increased from 0 to 20 mm and thereafter remained nearly constant. In contrast, the short axis increased continuously as the height increased from 0 mm to 250 mm. We show the representative long/short axis ratio of the particles collected at 0, 40 and 120 mm on the side collector in Figure 3b. The ratio of the particles of all sample were summarized in Figure S4. The size evolves because the number of cubic and polyhedral particles increases while the number of needle particles diminishes. Therefore, we measured the IR absorbance of the floating nanoparticles in the gas current around the evaporation source at different heights, and compared the spectra with the ex-situ IR spectra of the collected particles.

To demonstrate the evolution of the IR spectra of the nucleated molybdenum oxide nanoparticles, we conducted two experimental runs (A and B) under the same conditions. In Experiment A, we surveyed from 10 mm below to 10 mm above the evaporation source (Figure 4A1-5). In Experiment B,

we scanned the growth of nanoparticles in the smoke from 7.5 mm to 67.5 mm above the evaporation source (Figure 4B1-13). Once the temperature of the evaporation source had stabilized, the scan was started in the upward direction. When the scan reached the top in each experiment, it was returned to the starting position and proceeded downward. Figure 4 shows the spectra measured in the downward direction. At any given distance from the evaporation source, the same spectral features were observed in the upward direction (Figure S5). The IR evolution shows a clear spatial dependence. The spectra measured at 10 mm above the evaporation source in Experiment A (Figure 4A5) were identical to those measured at 7.5 mm above the evaporation source in Experiment B (Figure 4B1). The shape of the IR absorption band continuously changed from 10 mm beneath the evaporation source to 67.5 mm above the evaporation source. The swell in the 1000–750 cm^{-1} region is contributed by at least six subtle absorptions (indicated by the blue lines in Figure 4). The combination of these subtle absorptions alters the shape of the IR spectra in that region from singly to doubly peaked.

The spectral features were compared with those obtained by ex-situ IR measurements of nanoparticles collected at the same height and embedded into KBr pellets (Figure 4K1, K2; Figure S6). In the ex-situ IR spectrum of the needle particles collected on the side collector at 0 mm, the strongest absorption appears at 860 cm^{-1}. A single swell in the 1000–750 cm^{-1} region also appears. In contrast, the ex-situ IR spectrum of the cubic nanoparticles collected at ~250 mm exhibits peaks at 880 and 780 cm^{-1}, and a double-swell in the 1000–750 cm^{-1} region. With increasing collection height, the in-situ IR spectra undergo a transition from the single- to double-swell absorptions, consistent with the ex-situ IR measurements. Note that the IR spectral features are influenced by electromagnetic interactions between the particles and the embedding KBr medium.[30] Therefore, the peak positions are shifted toward lower wavenumbers, and the band widths are larger, than in IR spectra measured in the free-flying state. Despite these differences, the whole profile of the absorption, including the single and double swells, reflects the shape of MoO_3 nanoparticles. We conclude that the collected particles were frozen and their characteristics were negligibly changed after deposition on the side and top collectors.

The whole profile of the IR spectra is dominated by the superposition of sub-peaks at 1000–750 cm^{-1}, which have been suggested to arise from Mo–O stretching vibrations.[29] The relative intensities of the sub-peaks depend on the crystallographic anisotropy of the nanoparticles. The in-situ FT-IR measurements of the just-nucleated nanoparticles show peak in the 1000–750 cm^{-1} region, with the strongest absorption at 840 cm^{-1} (Figure 4). As the nanoparticles cool in the ascending gas current, the peaks at 900 and 910 cm^{-1} are gradually enlarged, whereas the peaks at 970 and 860 cm^{-1} in spectrum A1 are reduced in spectrum B13. The characteristic absorptions at 970 and 860 cm^{-1} of the just-nucleated nanoparticles are attributable to needle particles, and the relatively strong absorptions at 920, 910, 900 and 840 cm^{-1} are attributable to cubic and/or polyhedral particles.
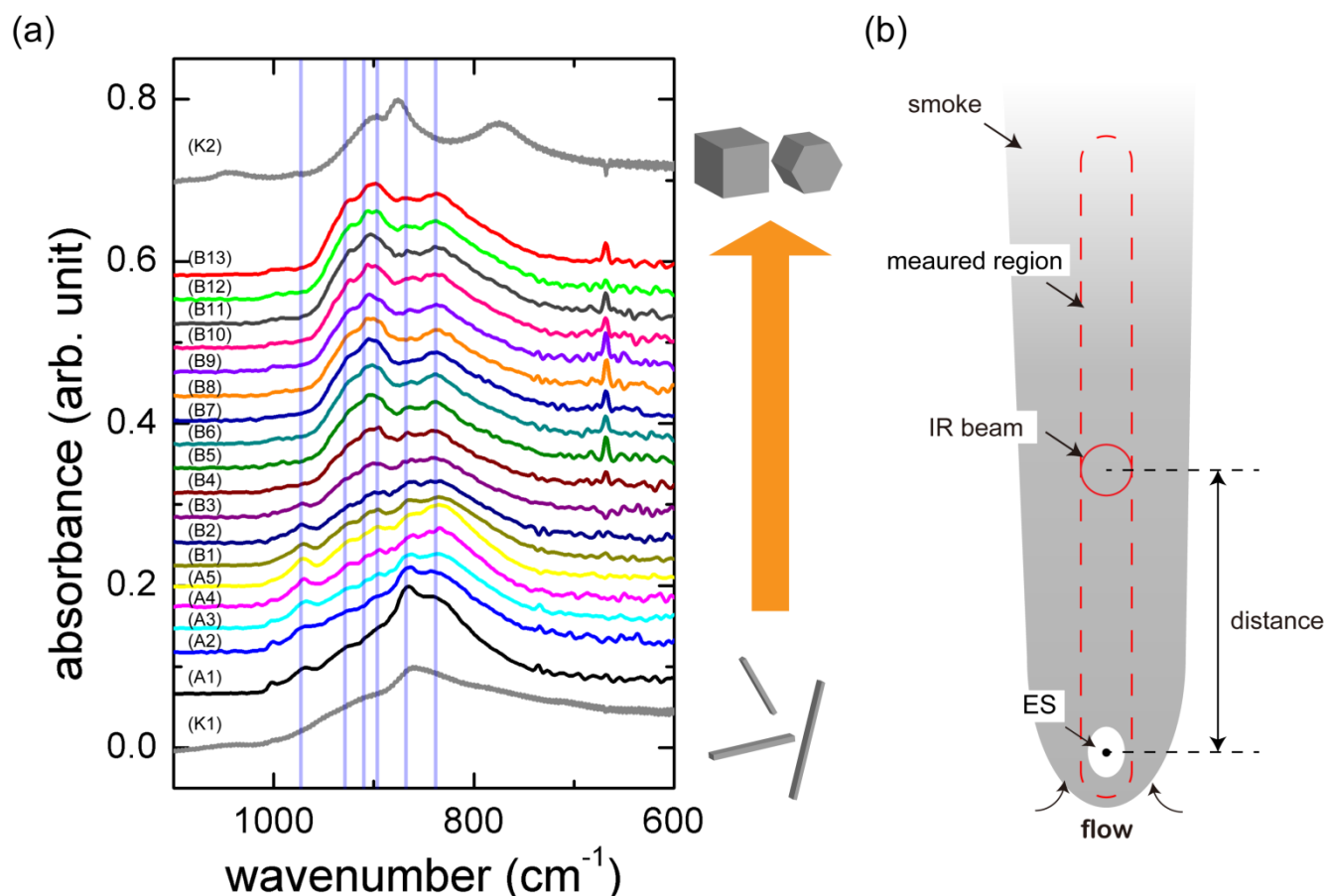
(a)

(b)

Figure 4. In-situ FT-IR spectra of nucleating and growing nanoparticles in a gas current (a) and a schematic view of the experiment along the evaporation source (ES) (b). In Experiment A, spectra were measured at 10 mm (A1) and 5 mm (A2) beneath the evaporation source, and at 0 mm (A3), 5 mm (A4), and 10 mm (A5) above the evaporation source. In Experiment B, they were measured at 7.5 (B1), 12.5 (B2), 17.5 (B3), 22.5 (B4), 27.5 (B5), 32.5 (B6), 37.5 (B7), 42.5 (B8), 47.5 (B9), 52.5 (B10), 57.5 (B11), 62.5 (B12) and 67.5 mm (B13) above the evaporation source. All spectra were obtained in the downward direction. Blue lines indicate the peaks at 970, 920, 910, 900, 860 and 840 cm^{-1}. The spectra labeled K1 and K2 are the IR spectra of the needle particles and the cubic/polyhedral particles, respectively, measured by the KBr embedding method.

Discussions

We have questioned how the needle particles transform into cubic and polyhedral particles in the ascending gas current. In our experimental set up, the evaporant flowed by convection and is quenched at temperature gradients >1000 K s^{-1}. The observed characteristic features of the just-nucleated nanoparticles were attributed to the needle-shaped molybdenum oxide (spectrum A1 in Figure 4). In previous studies, we determined the partial pressure of the source molecules at the nucleation point as ~10^3 Pa.[19–21] In such an atmosphere, a nanoparticle grows to several tens of nanometers in 10^{-3} s,[19,20] with simultaneous consumption of the vaporized source molecules. The time scale of vapor growth is several orders of magnitude faster than the time scale of convection (~1 s from the evaporation source to the top of the chamber, estimated from the convection of visible smoke). In addition, the MoO$_3$ vapor pressure at more than 5 mm above the evaporation source, estimated from temperature fields derived from thermocouple data (Figure S7), is <10^{-6} Pa. Thus, the vapor growth by molecular consumption should finish immediately after nucleation, which

initiates within several millimeters of the evaporation source. The nanoparticles are needle-shaped by anisotropic vapor growth. In our previous experiments, nucleation of the non-crystalline precursor was revealed in the IR spectra of Al$_2$O$_3$ and TiO$_2$.[28,31] As the IR spectrum of the just-nucleated nanoparticles already reveals monoclinic crystal formation and differs from that of non-crystalline particles, the phase transition from non-crystalline to crystalline form may occur earlier than the time scale of vapor growth. However, direct nucleation of crystalline particles from the evaporated vapor cannot be excluded from the possible formation pathway.

In-situ measurement revealed that the needle nanocrystals evolved into cubic and polyhedral nanocrystals at more than 10 mm above the evaporation source. In addition, the IR spectral features of the collected nanoparticles transited from single- to double-swell, even in the 50–250 mm region. The temperature variation at increasing vertical distance from the evaporation source (which was maintained at 1900 ± 100 K) was measured by a K-type thermocouple (Figure S7). The gas temperature of the growing region was below 673 K,[32] and the vapor pressure of MoO$_3$ was below 10^{-6} Pa. The size evolution along the short axis of the collected nanoparticles also revealed that growth proceeded under extremely low vapor

343 pressure conditions. This strongly suggests that the growth
344 and transformation are induced by coalescence, because no
345 growth units remained in the vapor at such low temperatures.
346 According to the size distributions of the particles collected at
347 different heights, the number of needle particles decreased at
348 higher collection points, while the number of cubic/polyhedral
349 particles increased. This indicates an evolution from smaller to
350 larger particles with increasing distance from the evaporation
351 source (Figure 3b and Figure S4). Here particles with
352 short/long axis ratios above 0.8 and below 0.4 were defined as
353 cubic/polyhedral and needle-shaped, respectively. Cubic or
354 polyhedral particles with a relatively larger long axis than that
355 of needle particles were not observed. In addition, the number
356 of smaller cubic/polyhedral particles did not decline,
357 suggesting negligible growth by monomer attachment. All of
358 these results are consistent with the coalescence of needle
359 particles into cubic and polyhedral nanocrystals.

360   To compare the attachment number of the needle particles
361 required to construct a cubic crystal (~10 particles) with the
362 collision number in the free-flying state, we then estimated
363 the collision frequency between the needle particles in a
364 simple simulation, ignoring the decreased number density of
365 the needle crystals during coalescence. The partial pressure of
366 MoO$_3$ was set to its typical value at the nucleation point (10^3
367 Pa). At this pressure, the needle particles were sized at 50.9
368 nm × 16.0 nm and their number density was 3.5×10^{20} m^{-3}.
369 This suggests that the particles are free-flying over a (300 ×
370 300) nm^2 area. We carried out a simple 2D random walk
371 simulation (see Supplementary Information). The simulated
372 collision frequency between the needle particles was 10^6–10^8
373 s^{-1}, implying that the number of collisions between the needle
374 particles is several orders of magnitude larger than the
375 number of attachments required to grow a cubic nanocrystal
376 from the needle particles. This implies that the needle particles
377 incorporate into the crystal only when their approach direction
378 aligns with the crystallographically equivalent planes. This
379 approach minimizes the total free energy of the resulting
380 particle, suggesting that newly approaching needle particles
381 preferentially incorporate into a kink site, as occurs in typical
382 crystals.

383   Needle particles were never randomly attached or
384 aggregated, nor elongated perpendicularly to the [011]
385 direction, over the cubic shape. Despite the most of the
386 resulting particles are transformed to cubic or polyhedral
387 shape, the number of the particles with the intermediate
388 short/long axis ratio (0.4-0.8) were relatively small in all
389 samples (Figure S4). Attachment probability of an intermediate
390 particle composed of several needle particles may be higher
391 than that of single needle particle because the intermediate
392 particle should have kink sites, or a few nanometer steps
393 between attached needle particles due to inhomogeneity of
394 the size of monomers (needle particles).

395   Aggregates of multiple needle particles with the same
396 crystallographic orientation were frequently observed in
397 samples collected at 20–80 mm above the evaporation source
398 (Figure S8). The ED patterns of single needle particles (Fig. 2b)
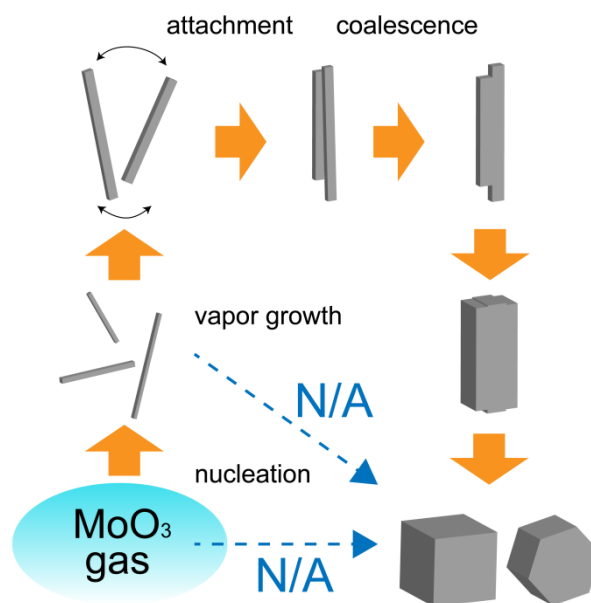399 are streaked in the [200] direction, evidencing that stacking

Figure 5. Schematic showing the shape evolution of just-nucleated MoO$_3$ nanoparticles in an ascending gas current. Previously considered mechanisms shown by dotted arrows (direct nucleation or monomer-by-monomer growth in vapor) are not applicable to the formation of cubic and polyhedral MoO$_3$ particles.

400 faults formed on (100). Owing to the attachments of the
401 needle particles, these stacking faults were periodic. Increased
402 structural defects caused by imperfect alignment during
403 oriented attachment has been reported in previous
404 studies.[23,25] Therefore, cubic and polyhedral particles probably
405 form by coalescence between the needle particles in planes
406 perpendicular to [011] in the ascending gas current.

407   The role of coalescence during frequent collisions in the
408 smoke of just-nucleated nanoparticles has been already
409 reported in the size evolution of metal and metal-oxide
410 nanoparticles. These collisions are thought to form connected
411 nanoparticles at surfaces, indicating that the molecules at the
412 surface of just-nucleated nanoparticles has significant
413 mobility.[32–34] The surface molecular diffusion may form the
414 faceted shapes. Attachment in crystallographically favorable
415 orientations was previously recognized in limited temperature
416 regions, but was never thought to majorly affect the
417 morphology of nanoparticles. At the bulk surface of SnO$_2$,
418 nanorods rotate to fit an equivalent plane before inserting into
419 that plane, even in vaccuum.[35] Such coalescence induced by
420 grain rotation is widely recognized.[36] We conclude that
421 selective coalescence at the crystallographically equivalent
422 planes of the just-nucleated nanoparticles, namely, oriented
423 attachment, strongly influenced the resulting morphology in
424 our experiments. The formation sequence of cubic and
425 polyhedral MoO$_3$ particles in vapor is schematically illustrated
426 in Figure 5.

427   Oriented attachment growth is suggested to proceed by
428 three driving forces; a thermodynamic driving force that
429 reduces the energetic disadvantage at the surface, Coulombic
430 (electrostatic) interactions, and van der Waals interactions.
431 Competition between these forces, which depend on the
432 orientation and surrounding medium, obscures the driving
433 force of coalescence growth.[26] If the main driving force arises

from thermodynamic requirement, a particle collides at the edge of another particle should be incorporated to reduce the energetic disadvantage at free surface. None of the needle particles aggregated in random orientations or in inequivalent planes suggests collision among particles always occurs at the central part of another particle. In contrast, Coulombic force interacts between particles and may attract each other at the central part, leading attachment at the near center. In aqueous solution, Coulombic interactions between particles decay exponentially with distance, as they are mediated by the ionic screening effect. Elimination of interfacial solvent molecules also influences the growth process. In addition, the surface energy differences between the planes are reduced in aqueous solution. In some simulation studies, the coalescence mechanisms of nanoparticles clearly differed in vacuum and solution. [26,27] Comparisons between these processes might elucidate the driving force of oriented attachment. In our experiments, large differences of surface energy between the fresh planes of the just-nucleated nanoparticles were expected, and the Coulombic forces should extend over much larger distances than in aqueous solution.

We present the first experimental report on the oriented attachment of free-flying nanoparticles in vapor. Such self-assembly growth in vapor is potentially applicable to industrial synthesis processes, and might explain natural mineral evolution such as cosmic dust aggregation during planet formation.[37] In the present experimental setup, we cannot distinguish between free-flying particles that have attached after electrostatic alignment and particles that have randomly attached, then immediately aligned to reduce the misfit.

In the previous consensus view, homogeneous nucleation from vapor occurs by a direct monomer-by-monomer process from molecules to crystals. However, our previous works revealed that metal-oxide nanoparticles crystallize by multistep processes.[28,31,38] The present study reveals a growth pathway of nanoparticles via oriented attachment, which has never been considered in nucleation and subsequent growth processes in vapor. These findings suggest that the versatile nucleation and growth pathways demonstrated in solution systems throughout the past decade also occur in vapor systems.

Conclusions

We measured the IR spectra during the formation of final crystals from homogeneously distributed just-nucleated MgO crystals in a highly supersaturated vapor. The crystals grew by oriented attachment. In the first step, needle particles form by anisotropic vapor growth around the evaporation source. The size of the critical nucleus was estimated as fewer than tens of molecules. The nuclei grew rapidly, forming 10-nm-scale needles in 0.1 s while rapidly exhausting the source gas. The free-flying needle particles collided in approximately 1 s. Finally, the needle particles attached in crystallographically equivalent planes, forming cubic and polyhedral nanoparticles. Attachment in crystallographically favorable orientations, which has not been previously recognized in nanoparticle formation in vapor, critically determines the properties of the resulting particles and is comparable to the typical growth process of macromolecular crystals. In this case, the growth units are the needle particles. This result provides new insights into the control of chemical compositions, morphologies, and polymorphs of industrial nanomaterials, and assists our understanding of cosmic dust aggregation in early solar systems.

Notes and references

1   S.-Y. Chung, Y.-M. Kim, J.-G. Kim and Y.-J. Kim, *Nat. Phys.*, 2009, **5**, 68–73.

2   A. E. S. Van Driessche, L. G. Benning, J. D. Rodriguez-Blanco, M. Ossorio, P. Bots and J. M. Garcia-Ruiz, *Science*, 2012, **336**, 69–72.

3   M. H. Nielsen, S. Aloni and J. J. De Yoreo, *Science*, 2013, **218**, 213–218.

4   D. C. Gary, M. W. Terban, S. J. L. Billinge and B. M. Cossairt, *Chem. Mater.*, 2015, **27**, 1432–1441.

5   J. Baumgartner, A. Dey, P. H. H. Bomans, C. Le Coadou, P. Fratzl, N. A. J. M. Sommerdijk and D. Faivre, *Nat. Mater.*, 2013, **12**, 310–314.

6   D. Loh, S. Sen, M. Bosman, S. F. Tan, J. Zhong, C. A. Nijhuis, P. Kral, P. Matsudaira and U. Mirsaidov, *Nat. Chem.*, 2016, 1–10.

7   M. K. Bera and M. R. Antonio, *J. Am. Chem. Soc.*, 2016, **138**, 7282–7288.

8   C. J. S. Ibsen, D. Gebauer and H. Birkedal, *Chem. Mater.*, 2016, **28**, 8550–8555.

9   S. Parveen, R. J. Davey, G. Dent and R. G. Pritchard, *Chem. Commun. (Camb).*, 2005, 1531–1533.

10   K. Harano, T. Homma, Y. Niimi, M. Koshino, K. Suenaga, L. Leibler and E. Nakamura, *Nat. Mater.*, 2012, **11**, 877–881.

11   C. Sun and D. Xue, *Cryst. Growth Des.*, 2015, **15**, 2867–2873.

12   P. G. Vekilov, *Nanoscale*, 2010, **2**, 2346–2357.

13   T. Yamazaki, Y. Kimura, P. G. Vekilov, E. Furukawa, M. Shirai, H. Matsumoto, A. E. S. Van Driessche and K. Tsukamoto, *Proc. Natl. Acad. Sci.*, 2017, **114**, 201606948.

14   T. H. Zhang and X. Y. Liu, *J. Phys. Chem. B*, 2007, **111**, 14001–14005.

15   J. R. Savage and A. D. Dinsmore, *Phys. Rev. Lett.*, 2009, **102**, 15–18.

16   W. Ostwald, *Zeitschrift für Phys. Chemie*, 1897, **22**, 289–302.

17   D. Chakraborty and G. N. Patey, *J. Phys. Chem. Lett.*, 2013, **4**, 573–578.

18   J. Ihli, W. C. Wong, E. H. Noel, Y.-Y. Kim, A. N. Kulak, H. K. Christenson, M. J. Duer and F. C. Meldrum, *Nat. Commun.*, 2014, **5**, 3169.

19   Y. Kimura, H. Miura, K. Tsukamoto, C. Li and T. Maki, *J. Cryst. Growth*, 2011, **316**, 196–200.

20   Y. Kimura, K. K. Tanaka, H. Miura and K. Tsukamoto, *Cryst. Growth Des.*, 2012, **12**, 3278–3284.

21   Y. Kimura, K. K. Tanaka, T. Nozawa, S. Takeuchi and Y. Inatomi, *Sci. Adv.*, 2017, **3**, e1601992.

22   N. T. K. Thanh, N. Maclean and S. Mahiddine, *Chem. Rev.*, 2014, **114**, 7610–7630.

23   R. L. Penn and J. F. Banfield, *Science*, 1998, **281**, 969–971.

24   J. F. Banfield, *Science*, 2000, **289**, 751–754.

25   D. Li, M. H. Nielsen, J. R. I. Lee, C. Frandsen, J. F. Banfield and J. J. De Yoreo, *Science*, 2012, **336**, 1014–1018.

26   H. Zhang and J. F. Banfield, *CrystEngComm*, 2014, **16**, 1568–1578.

27   M. Raju, A. C. T. Van Duin and K. A. Fichthorn, *Nano Lett.*, 2014, **14**, 1836–1842.

28   S. Ishizuka, Y. Kimura, T. Yamazaki, T. Hama, N. Watanabe and A. Kouchi, *Chem. Mater.*, 2016, **28**, 8732–8741.

29   M. Kurumada and C. Kaito, *J. Phys. Soc. Japan*, 2006, **75**, 2–6.

30   C. F. Bohren and D. R. Huffman, *Absorption and Scattering of Light by Small Particles*, John Wiley & Sons., New York, United States, 1983.

31   S. Ishizuka, Y. Kimura and T. Yamazaki, *J. Cryst. Growth*, 2016, **450**, 168–173.

32   C. Kaito, *Jpn. J. Appl. Phys.*, 1978, **17**, 601–609.

33   C. Kaito, *Jpn. J. Appl. Phys.*, 1985, **24**, 261–264.

34   O. Kido, H. Suzuki, Y. Saito and C. Kaito, *Jpn. J. Appl. Phys.*, 2003, **42**, 5705–5708.

35   C. Ribeiro, E. J. H. Lee, T. R. Giraldi, R. Aguiar, E. Longo and E. R. Leite, *J. Appl. Phys.*, 2005, **97**, 24313.

36   D. Moldovan, V. Yamakov, D. Wolf and S. R. Phillpot, *Phys. Rev. Lett.*, 2002, **89**, 206101.

37   S. Okuzumi, M. Momose, S. Sirono, H. Kobayashi and H. Tanaka, *Astrophys. J.*, 2016, **821**, 82.

38   S. Ishizuka, Y. Kimura and I. Sakon, *Astrophys. J.*, 2015, **803**, 88.